Influence of ligand field on magnetic anisotropy in a family of pentacoordinate Co complexes

Joydev Acharya, Arup Sarkar, Pawan Kumar, Vierandra Kumar, Jessica Flores Gonzalez, Olivier Cador, Fabrice Pointillart, Gopalan Rajaraman, Vadapalli Chandrasekhar

Influence of Ligand Field on Magnetic Anisotropy in a Family of Pentacoordinate Co^{II} Complexes

Joydev Acharya,[a] *Arup Sarkar,*[b] *Pawan Kumar,*[a] *Vierandra Kumar,*[a] *Jessica Flores Gonzalez,*[c] *Olivier Cador,*[c] *Fabrice Pointillart,**[c] *Gopalan Rajaraman,**[b] *and Vadapalli Chandrasekhar**[a,d]

[a]Department of Chemistry, Indian Institute of Technology Kanpur, Kanpur-208016, India. E-mail: vc@iitk.ac.in, http://www.iitk.ac.in

[b]Department of Chemistry, Indian Institute of Technology Bombay, Powai, Mumbai-400 076, India. E-mail: rajaraman@chem.iitb.ac.in

[c]Univ Rennes, CNRS, ISCR (Institut des Sciences Chimiques de Rennes) - UMR 6226, F-35000 Rennes, France E-mail: fabrice.pointillart@univ-rennes1.fr

[d]Tata Institute of Fundamental Research, 36/P, Gopanpally Village, Serilingampally Mandal, Ranga Reddy District, Hyderabad 500107, India.

Abstract

A family of mononuclear penta-coordinated Co^{II} complexes, $[Co(L)Cl_2]\cdot CH_3OH$ (**1**), $[Co(L)Br_2]$ (**2**) and $[Co(L)(NCS)_2]$ (**3**) (where L is 1-mesityl-*N*,*N*-bis(pyridin-2-ylmethyl)methanamine) were synthesized and characterized. In these complexes, the neutral non-planar ligand, L, binds to three coordination sites around the metal center while two others are bound by anionic halide/pseudo halide ligands. The coordination geometry of the complexes is dictated by the coordinated anionic ligands. Thus, the coordination geometry around the metal ion is distorted trigonal bipyramidal for complexes **1** and **3**, while it is distorted square pyramidal for complex **2**. *Ab initio* CASSCF/NEVPT2 calculations on the complexes reveal the presence of an easy plane magnetic anisotropy with the *D* and *E/D* values being, 13.3 and 0.14 cm^{-1} for **1**; 36.1 and 0.24 cm^{-1} for **2** and ±8.6 and 0.32 cm^{-1} for **3**. These values are in good agreement with the values that were extracted from the experimental DC data. AC magnetic measurements reveal the presence of a field-induced slow relaxation of magnetization. However, clear maxima in the out-of-phase susceptibility curves were not observed for **1** and **3.** For complex **2**, peak maxima were observed when the measurements were carried out under an applied field of 1400 Oe which allowed an analysis of the dynamics of the slow relaxation of magnetization. This revealed that the relaxation is mainly controlled by the *Raman* and *Direct* processes with the values of the parameters found to be: $B = 0.77(15)\ s^{-1}K^{-6.35}$, n = 6.35(12) and $A = 3.41(4)\cdot 10^{-10}\ s^{-1}Oe^{-4}K^{-1}$ and m = 4 (fixed). The *ab initio* calculation which showed the multifunctional nature of the electronic states of the complexes justifies the absence of zero-field SIM behaviour of the complexes. The magnitude and sign of the *D* and *E* values and their relationship with the covalency of the metal-ligand bonds was analysed by the CASSCF/NEVPT2 as well as AILFT calculations.

Introduction

Single molecule magnets (SMMs) containing single paramagnetic centres have been receiving considerable interest in recent years.[1-6] Such complexes, also known as single-ion magnets (SIMs), are a late entry into the family of molecule-based magnets, a field that began with the discovery of this property in the dodecanuclear mixed-valent manganese complex $[Mn_{12}O_{12}(CH_3COO)_{16}(H_2O)_4]$.[7, 8] Because of the presence of a large number of paramagnetic metal ions within this complex whose interaction resulted in an overall ground state spin, S = 10, initial focus in this area was on preparing polynuclear metal ensembles possessing a large number of paramagnetic metal ions. These early studies have also led to the realization that SMMs, once magnetized, possess a barrier height (U_{eff}) for spin reversal. The magnitude of U_{eff} was found to be proportional to $|D|S^2$ for integral spin values and $|D|(S^2 - ¼)$ for non-integral spin values, where S equals the net ground state spin while D is related to the negative uniaxial magnetic anisotropy. While the initial efforts were mainly on increasing S, it was soon realised that there exists an inverse relation between S and D thereby resulting in situations where gains made in S are lost because of diminishing D. It was around this time, in 2003, that a seminal discovery was reported by Ishikawa and co-workers who disclosed that the mononuclear sandwich complex, bis(phthalocyaninato)terbium(III) was a SIM because of the presence of an inherent, large, unquenched orbital angular momentum in lanthanide ions.[9] This discovery allowed synthetic chemists to design mononuclear complexes where the metal ion, either as a result of its coordination geometry or/and because of its inherent nature, would contribute to significant spin-orbit coupling. Long and co-workers summarized a qualitative method for predicting the ligand field that will maximize the magnetic anisotropy for lanthanide ions. Thus, an axial coordination for oblate Dy^{III} and Tb^{III} ions, and an equatorial coordination for prolate ions like Yb^{III} and Er^{III} would be preferred to stabilize an Ising type magnetic anisotropy.[10] These predictions were vindicated

in mononuclear lanthanide complexes, such as $[[(^{t}BuPO(NH^{i}Pr)_2)]_2Dy(H_2O)_5][I]_3]$,[11] $[Dy(O^{t}Bu)_2(py)_5][BPh_4]$[12], $[Dy(Cp^{ttt})_2][B(C_6F_5)_4]$[13] and $[(Cp^{iPr5})Dy(Cp^*)]^+$ [14] or a series of dysprosium(III) metallocenium salts[6] which revealed excellent SIM characteristics. Simultaneously, there have also been efforts to examine if appropriate mononuclear transition metal complexes would also be able to behave as molecular magnets. Among the important examples of this genre[15-20] include the low-coordinate complexes $[(sIPr)Co^{II}NDmp]$,[21] $Co(C(SiMe_2ONaph)_3)_2$,[22] $[Fe(C(SiMe_3)_3)_2]_2^-$, [23] and $[Ni(6\text{-}Mes)_2]Br$, [24]. The low coordination forces the *d* orbitals to stay within a narrow energy range, similar to the 4f orbitals of lanthanide complexes. Among the afore-mentioned low-coordinated transition metal examples, the Co^{II} ion, due to its high magnetic anisotropy arising from an unquenched spin-orbit coupling in the ground state and being a Kramers ion seems to be extremely suitable for the preparation of SIMs.[25, 26] Being a Kramers ion, Co^{II} would have a bistable ground electronic state, so, independent of the sign of $|D|$, its complexes can show slow relaxation of magnetization for a wide range of coordination numbers ranging from 2 to 8.[27-41] However, fine-tuning the coordination number and geometry of Co^{II} complexes to achieve significant magnetic properties is still a work in progress.

In this context, we disclose the preparation, structural investigation and a combined theoretical and experimental magnetic studies of a series of pentacoordinate Co^{II} complexes, $[Co(L)Cl_2]\cdot CH_3OH]$ (**1**), $[Co(L)(Br)_2]$ (**2**), $[Zn(L)_2Br_2]$ (**2_{Zn}**), $[Zn_{0.9}Co_{0.1}(L)(Br)_2]$ (**2_{10}**) and $[Co(L)(NCS)_2]$ (**3**). These complexes were prepared by using a di-(2-picolyl) amine-based tridentate ligand (L). One of the objectives of this study is to investigate the role of halide/pseudohalide ligands in controlling the geometry and magnetic behavior of the complexes. The experimental static and dynamic magnetic investigations of **1**-**3** were supplemented by theoretical studies.

Experimental Section

All the solvents were purified by adopting standard procedures.[42] The chemicals, $CoCl_2 \cdot 6H_2O$, $CoBr_2$, α^2-chloroisodurene (Sigma-Aldrich, USA) $Co(NCS)_2$ and di(2-picolyl)amine (TCI Chemicals (India) Pvt. Ltd.) were used as purchased.

Instrumentation

Melting points were measured using a JSGW melting point apparatus and are uncorrected. IR spectra were recorded as KBr pellets on a Bruker Vector 22 FT IR spectrophotometer operating at 400–4000 cm^{-1}. ^1H NMR spectra were recorded on a JEOL JNM LAMBDA 400 model spectrometer operating at 500 MHz. Chemical shifts are reported in parts per million (ppm) and are referenced with respect to internal tetramethylsilane (^1H). Elemental analyses of the compounds were obtained from Thermoquest CE instruments CHNS-O, EA/110 model. Electrospray ionization mass spectrometry (ESI-MS) spectra were recorded on a Micromass Quattro II triple quadrupole mass spectrometer. Ethanol was used as the solvent for the electrospray ionization (positive ion, full scan mode). Capillary voltage was maintained at 2 kV, and cone voltage was kept at 31 kV. Powder X-ray diffraction patterns were collected by PANalytical XPert Powder diffractometer with Cu-Kα as incident radiation (λ = 0.154 nm) in the 2θ range between 5° and 50° with step size of 0.01°. The samples were prepared by drop casting the acetonitrile suspension of crystals on glass slide followed by evaporation of solvent in open air.

The SCXRD data for the complexes **1** and **2** were collected on a Bruker SMART CCD diffractometer (MoKα radiation, λ = 0.71073 Å). Collecting frames of data, indexing reflections, and determining lattice parameters was done by the program SMART, integrating the intensity of reflections and scaling was done by SAINT[43], SADABS[44] for absorption

correction, and SHELXTL[45] for space group and structure determination and least-squares refinements on F^2. On the other hand X-ray diffraction data for complex **3** was collected at low temperature (120 K) by using Rigaku diffractometer with graphite-monochromated molybdenum Kα radiation, λ= 0.71073 Å. Data integration and reduction were processed with CrysAlisPro software.[46] An empirical absorption correction was applied to the collected reflections with SCALE3 ABSPACK integrated with CrysAlisPro. All the crystal structures were solved and refined by full-matrix least-squares methods against F^2 by using the program SHELXL-2014[47] using Olex^2 software [48]. All non-hydrogen atoms were refined with anisotropic displacement parameters. The position of the hydrogen atoms was fixed at calculated positions and refined isotropically thoroughly. The crystallographic Figures have been generated using Diamond 3.1e program.[49] The crystal data and the cell parameters for **1**−**3** are summarized in Table S2. Crystallographic data (excluding structure factors) for the structures of **1-3** and $\mathbf{1_{Zn}}$, $\mathbf{2_{Zn}}$ have been deposited with the Cambridge Crystallographic Data Centre as supplementary publication nos. CCDC 1950107-1950111 contain the supplementary crystallographic data for this paper. These data can be obtained free of charge via www.ccdc.cam.ac.uk/data_request/cif, or by emailing data_request@ccdc.cam.ac.uk, or by contacting The Cambridge Crystallographic Data Centre, 12 Union Road, Cambridge CB2 1EZ, UK; fax: +44 1223 336033.

The dc magnetic susceptibility measurements were performed on solid polycrystalline samples (the micro-crystallites are immobilized in pellets) with a Quantum Design MPMS-XL SQUID magnetometer between 2 and 300 K in the applied magnetic field of 2 kOe in the 2-20 K temperature range and 10 kOe above 20 K. All the measurements incorporated correction for the diamagnetic contribution as calculated with Pascal's constants. The ac magnetic susceptibility measurements were performed on Quantum Design MPMS-XL SQUID magnetometers.

Computational Methods

The Spin-Hamiltonian parameters were computed using *ab initio* CASSCF/NEVPT2 method on the X-Ray structures (**1**-**3**) using ORCA 4.0.1 programme.[50] Scalar relativistic Douglas-Kroll-Hess (DKH) Hamiltonian was used during all the calculations. Along with this DKH version of contracted basis sets- DKH-def2-TZVP for Co, Cl and Br; DKH-def2-TZVP(-f) for first coordination sphere atoms such as N and O; and DKH-def2-SVP for rest of the atoms were used throughout the calculations. The state average complete active space self-consistent field (SA-CASSCF) calculations were carried out in the active space of seven metal electrons in five 3d orbitals, i.e., CAS (7, 5) space and the wave functions were optimized with 10 quartets and 40 doublets. Dynamic electron correlation was also calculated on the top of CASSCF wave function using N-electron valence perturbation theory second order (NEVPT2) method. Spin-orbit coupling and final Spin-Hamiltonian parameters were computed using quasi-degenerate perturbation theory (QDPT) and universal effective Hamiltonian approach (EHA) respectively.[51] Furthermore, *ab initio* ligand field theory (AI-LFT) analysis has also been carried out considering 10 quartet roots only.

Synthesis

Synthesis of 1-mesityl-*N*,*N*-bis(pyridin-2-ylmethyl)methanamine (L)

To a 20 mL DMSO solution of KOH (1.13 g, 20.08 mmol) in a round bottom flask at room temperature was added di-(2-picolyl) amine (2.0 g, 10.04 mmol) and stirred for 2 hours generating a pink red solution. α^2-Chloroisodurene (1.69 g, 10.04 mmol) was added to the stirred pink red solution and again stirred for another 3 hours before the reaction was quenched by adding crunched ice. The organic part from the reaction mixture was separated after 3-4 extractions with diethyl ether (30 mL each time). The combined organic layer was dried over Na_2SO_4 before complete evaporation by rotary evaporator to get a semisolid white

product. The crude product was purified by column chromatography on silica gel using hexane-ethyl acetate (1:4) as an eluent in the form of white powder (2.66 g) in 80% yield. Anal. Calcd. for $C_{22}H_{25}N_3$ (331.2) C, 79.72; H, 7.6; N, 12.68. Found: C, 79.5; H, 7.86; N, 12.62. ^{1}H NMR ($CDCl_3$): δ = 8.43 (d, 2H, *o*-C_{py}-H), 7.56 (t, 2H, *p*-C_{py}-H), 7.35 (d, 2H, C_{py}-H), 7.06 (t, 2H, *m*-C_{py}-H), 6.7 (s, 2H, C_{Ar}-H), 3.69(s, 4H, -CH_2), 3.62 (s, 2H, -CH_2), 2.22 (s, 6H, Ar-CH_3), 2.14 (s, 3H, Ar-CH_3).

Synthesis of $[Co(L)Cl_2]\cdot CH_3OH$ (1)

To a stirred solution of the ligand, L (0.06 g, 0.181 mmol) in 30 mL CH_3CN was added solid $CoCl_2\cdot 6H_2O$ (0.043 g, 0.181 mmol) and stirred for 10 minutes in room temperature before being heated to reflux for 2 h. After cooling, the solvent was completely removed under reduced pressure and the blue residue was thoroughly washed with diethyl ether. The washed residue was dissolved in $CHCl_3$-CH_3OH mixture (3:1). Block-shaped blue crystals were obtained by diffusion of diethyl ether into the solution for 4-5 days at room temperature. Yield: 0.06 g (72%, based on the molecular weight of metal salt). M.P: 220 °C. Elemental analysis. Calcd (%): C, 56.00; H, 5.93; N, 8.52. Found: C 55.42, H 5.36, N 8.69; FT-IR (KBr) cm^{-1}: 3452 (b), 3029 (w), 2917 (w), 1607 (s), 1480 (s), 1021 (s), 771 (s).

Synthesis of $[Co(L)Br_2]$ (2)

A similar synthetic procedure was followed as for **1**, but $CoBr_2$ (0.04 g, 0.181 mmol) was used in place of $CoCl_2\cdot 6H_2O$ and the X-ray quality block-shaped blue crystals were grown by the similar process as described in case of **1**. Yield: 0.069 g (68.5%, based on the molecular weight of metal salt). M.P: >240 °C. Elemental analysis. Calcd (%):C, 48.03; H, 4.58;N, 7.64. Found: C 48.23, H 4.68, N 7.9; FT-IR (KBr) cm^{-1}: 3451 (b), 3072 (w), 2920 (w), 1607 (s), 1478 (s), 1439 (s), 1290 (s), 845(s).

Synthesis of $[Co(L)(NCS)_2]$ (3)

A similar synthetic procedure was followed as for **1**, but $Co(NCS)_2$ (0.032 g, 0.181 mmol) was used in place of $CoCl_2 \cdot 6H_2O$ and the X-ray quality block-shaped blue crystals were grown by the similar process as described in case of **1**. Yield: 0.0518 g (56%, based on the molecular weight of metal salt). M.P: >225 °C. Elemental analysis. Calcd (%):C, 56.91; H, 4.97; N, 13.83. Found: C 57.11, H 4.74, N 13.92; FT-IR (KBr) cm^{-1}: 3455 (b), 3080 (w), 2918(w), 2071(s), 1607.94 (s), 1480 (s), 1445 (s), 1055 (w), 1027(w), 765(s).

Synthesis of $[Zn(L)_2Br_2]$ ($\mathbf{2_{Zn}}$)

A similar synthetic procedure was adapted as for **2**, but $ZnBr_2$ (0.041 g, 0.181 mmol) was used instead of $CoBr_2$. Yield: 0.069 g (68 % based on the molecular weight of metal salt). Elemental analysis. Calcd (%): C 47.47, H 4.53, N 7.55. Found: C 48.01, H 4.64, N 7.33. FT-IR (KBr) cm^{-1}: 3453 (b), 3070 (w), 2918 (w), 1609 (s), 1475 (s), 1433 (s), 1294 (s), 843(s)

Single crystal XRD measurement was done on $\mathbf{2_{Zn}}$. The unit cell measurement revealed that $\mathbf{2_{Zn}}$, has similar unit cell parameters and packing pattern like in **2**. Thus, they were used as diamagnetic matrixes to host the corresponding paramagnetic Co^{II} analogues of **2**. To have further evidence, we performed powder X-ray diffraction measurement for $\mathbf{2_{Zn}}$ to gain more experimental proof to support the fact and found sufficiently good agreement with the simulated data obtained from single-crystal data of the corresponding Co^{II} analogues (see Figures S17-S19 in Supporting Information).

Preparation of 10 % diluted sample of 2 ($\mathbf{2_{10}}$)

To a stirred solution of ligand, L (0.06 g, 0.181 mmol) in 30 mL CH_3CN was added solid $CoBr_2$ (0.0043 g, 0.0181 mmol) and $ZnBr_2$ (0.037 g, 0.1629 mmol) and stirred for 10 minutes in room temperature before heating to reflux for 2 h. After cooling the solvent was

completely removed under reduced pressure and the blue residue was thoroughly washed with diethyl ether. The washed residue was dissolved in $CHCl_3$-CH_3OH mixture (3:1). Block-shaped blue crystals were obtained by diffusion of diethyl ether into the solution for 4-5 days at room temperature.

Results and Discussion

Synthesis

From literature, it is seen that neutral tridentate ligands are widely used for synthesizing five-coordinated transition metal complexes including those involving Co^{II}.[52-54] Keeping this in mind we designed a di-(2-picolyl)amine-based non-planar, flexible, tridentate ligand (L) having only *N* donor sites. The synthesis of L was accomplished by the reaction of di-picolylamine with α^2-chloroisodurene. The reaction of L with $CoCl_2 \cdot 6H_2O$ or MBr_2 (M = Co and Zn), or $Co(NCS)_2$ in a 1:1 stoichiometric ratio in CH_3CN, under reflux, afforded $(Co(L)Cl_2 \cdot CH_3OH]$ (**1**); $[Co(L)Br_2]$ (**2**), $[Zn(L)Br_2]$ (**2_{Zn}**) and $[Co(L)(NCS)_2]$ (**3**) respectively (Scheme 1).

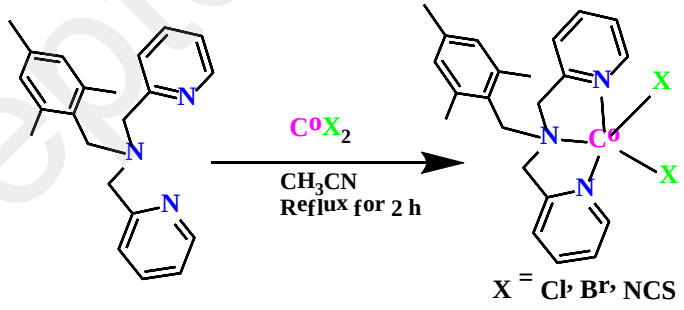

Scheme 1. Synthesis of **1-3**.

In order to check the structural integrity of the complexes in solution, ESI-MS studies were carried out. While in all cases the most abundant peak is represented by the fragment $[L+H]^+$,

other peaks containing both the ligand and the metal were found (Figures S1, S2). However, the parent ion peaks could not be found in any instance.

X-ray crystallography of 1–3

Single crystal studies on the three complexes reveal that **1** crystallizes in the monoclinic $P2_1/n$ space group while **2** and **3** crystallize in the triclinic $P\bar{1}$ space group. All the complexes are neutral and are five-coordinate. The central Co^{II} atom is coordinated to three nitrogen atoms from L and to two halides/pseudo-halides (Figure 2). In order to find the exact geometry and evaluate the magnitude of distortion around the metal ion in the complexes, we did the continuous 'SHAPE' measurement[55, 56] (see Supporting Information) and plotted 'CShM' values against all the possible geometries for five-coordinate species (Figure 1). This analysis indicates that the coordination geometry in **1** and **3** is closer to the trigonal bipyramid (TBPY-5) while the geometry in **2** is closer to the square pyramid (SPY-5).

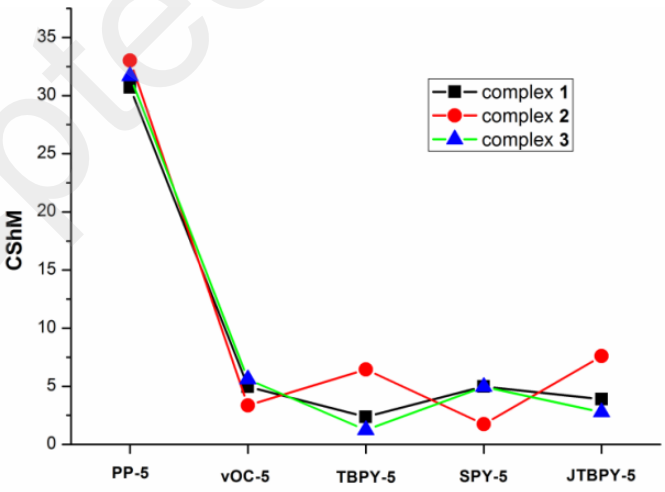

Figure 1. Plot of 'CShM' values from 'SHAPE' measurement against all possible geometries for five co-ordinate species.

In complex **1**, the axial positions are occupied by Cl2 and N2 while the equatorial positions are occupied by N1, N3, and Cl1 (Figure 2). The axial Cl2-Co-N2 bond angle is 169.4(4)˚ which deviates from the ideal bond angle of 180˚. The equatorial bond angles, N1-Co-Cl1(136.1(4)˚); N3-Co-Cl1 (103.5(5)˚); and N1-Co-N3(113.2(6)˚) also deviate from the ideal value of 120˚(see Table S1). The Co-Cl1 bond distance is 2.289(5) Å and is shorter than the Co-Cl2 bond distance (2.322(6) Å). Similarly, variations in the bond distance are seen among the Co-N bonds (Co-N1, 2.067(2) Å, Co-N2, 2.243(1) Å, Co-N3, 2.069(2) Å). In comparison to **1**, the geometry in **3** is found to be closer to the TBP geometry. Thus, the axial N2-Co-N5 bond angle is 172.4(6) ˚ while the equatorial bond angles are: N1-Co-N3, 115.8(6) ˚; N3-Co-N4, (105.9(6)˚ ; N1-Co-N4, (129.9(6)˚. Among the Co-N bond distances, the axial distances involving Co-N2 and Co-N5 are 2.301(2) Å and 2.026(2) Å while the equatorial distances, Co-N1, Co-N3, and Co-N4 are 2.039(1) Å, 2.061(1) Å, and 1.984(2) Å respectively.

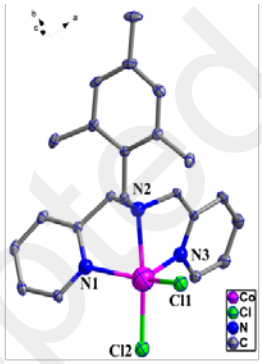

(a)

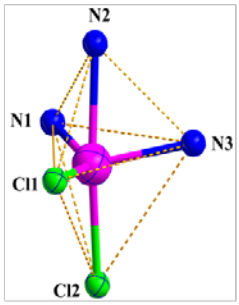

(b)

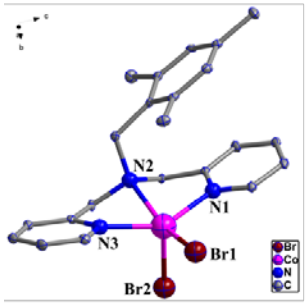

(c)

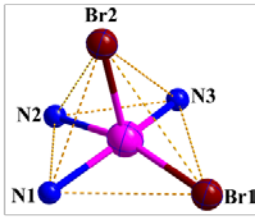

(d)

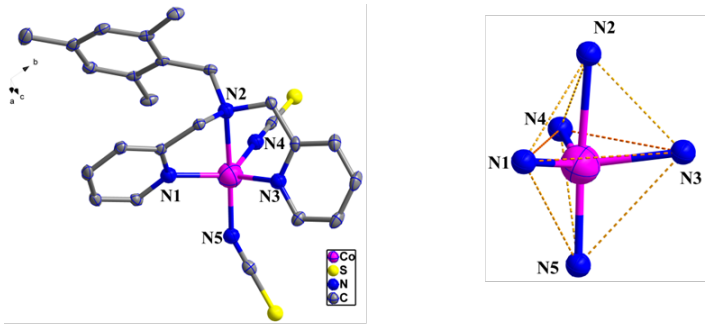

(e) (f)

Figure 2. (a) The molecular structure of **1**, (b) coordination geometry around **1**, (c) the molecular structure of **2**, (c) geometry around **2**, (e) the molecular structure of **3** and (f) geometry around **3**. Solvent molecules and hydrogen atoms are removes for the sake of clarity. Ellipsoids are drawn at 40% probability.

Unlike in **1** and **3**, in **2**, the geometry is distorted square pyramidal. The basal plane consists of three nitrogen and one bromide (Br1) centres. The only apical position is occupied by a bromide ion (Br2). The Co-N bond distances are Co-N1, 2.062(3) Å; Co-N2, 2.314(2) Å, and Co-N3, 2.079(3) Å. Among the two Co-Br bonds, the apical Co-Br2 bond (2.495(7) Å) is found to be longer than the equatorial Co-Br1 bond (2.439(6) Å).

In complex **2** the pyridine rings of the ligand of the adjacent molecules are seen to be stacked via a 'parallel face-centred $\pi\cdots\pi$ interaction' [57] (Figure 3).

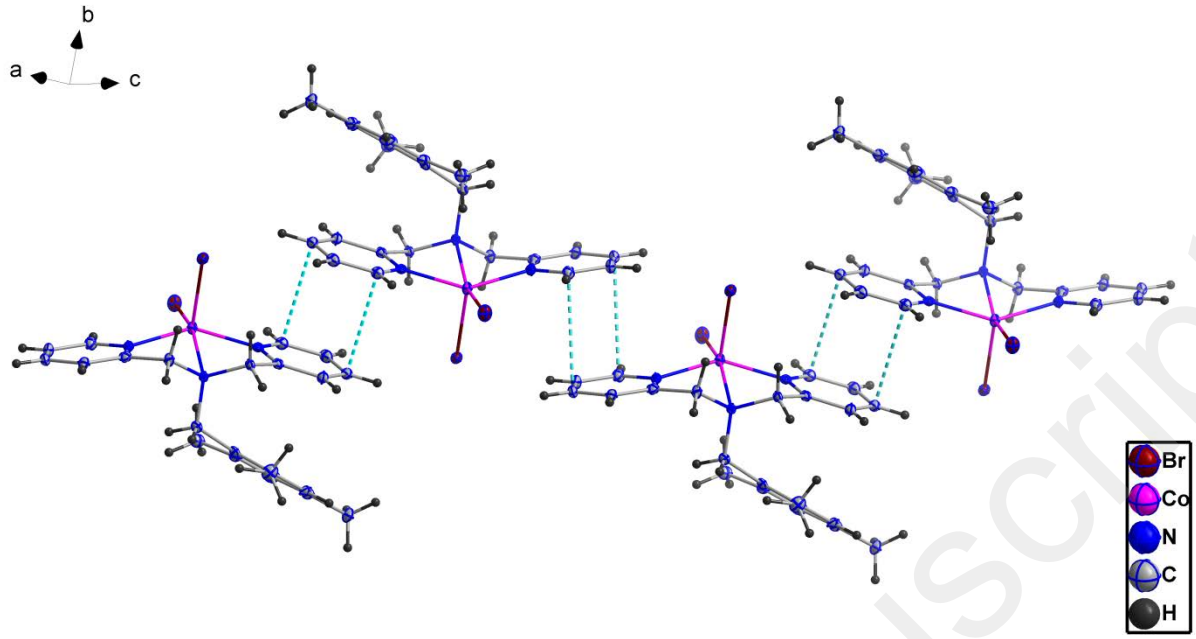

Figure 3. Parallel face-centered $\pi\cdots\pi$ interaction in **2** (shown in turquoise colour dotted bond). Ellipsoids are drawn at 40% probability.

Close observation of the packing pattern of all three complexes (**1**−**3**) revealed that the closest $Co^{II}\cdots Co^{II}$ distances are 7.876(6), 7.926(7), and 6.684(4) Å respectively (Figure 4).

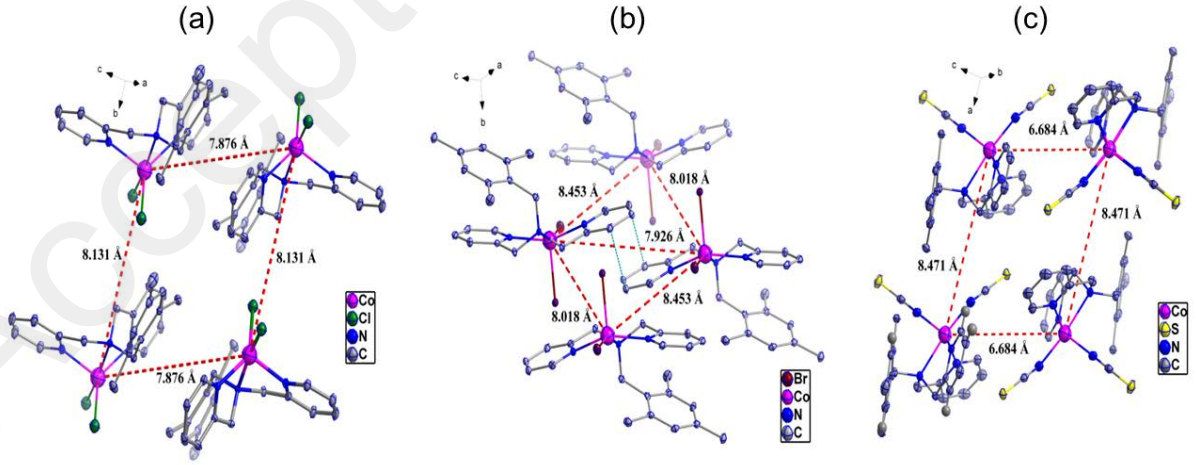

Figure 4. Simplified packing diagram (a) for **1**, (b) for **2**, (c) for **3** also showing intermolecular $Co^{II}\cdots Co^{II}$ distances. Ellipsoids are drawn at 40% probability.

Magnetic Properties of 1-3

The $\chi_M T$ vs. T plots (χ_M the molar magnetic susceptibility and T, the temperature expressed in Kelvin) of compounds **1-3** are represented in Figure 5. The room temperature values are equal to 2.6, 2.79 and 2.52 cm^3Kmol^{-1} for **1** to **3** respectively, in fairly good agreement with commonly observed values for Co^{II} in pentacoordinate environment [58] and higher than expected for S = $^3/_2$ spin only system (1.88 cm^3 K mol^{-1}). On cooling, $\chi_M T$ decreases monotonically due to the depopulation of S = $^3/_2$ sublevel and/or temperature-independent paramagnetism (TIP) which is taken into consideration when the data are fitted (*vide infra*) with a steepest decrease below 50 K (Figure 5). It must be noted that TIP can contain imperfect diamagnetic corrections. The low temperature (2 K) values are equal to 1.32, 1.47 and 1.67 cm^3 K mol^{-1}. The magnetization curves for all three complexes at 2 K do not saturate up to 50 kOe. At higher fields than 20 kOe the magnetization increases linearly which might indicate the presence of low-lying states.

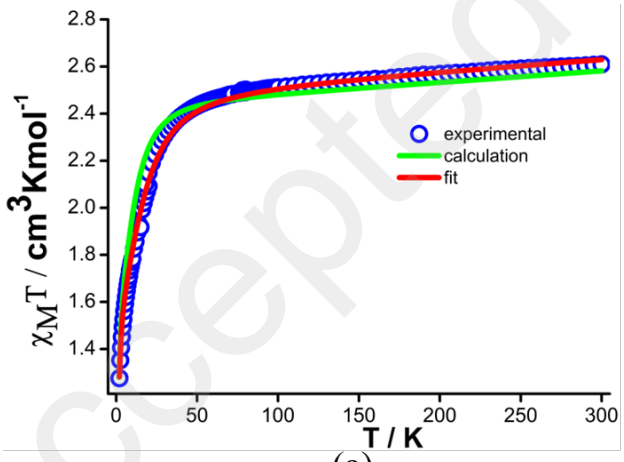

(a)

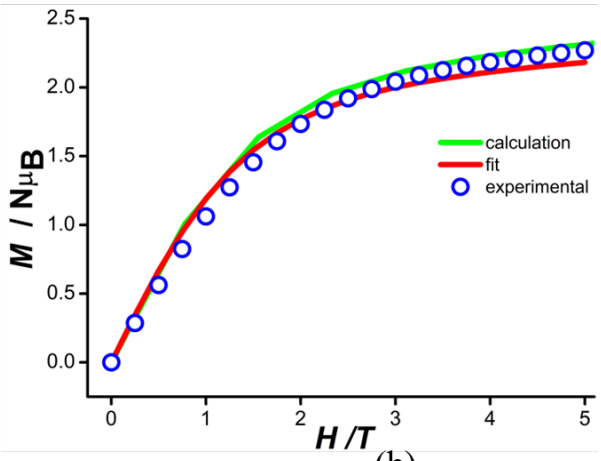

(b)

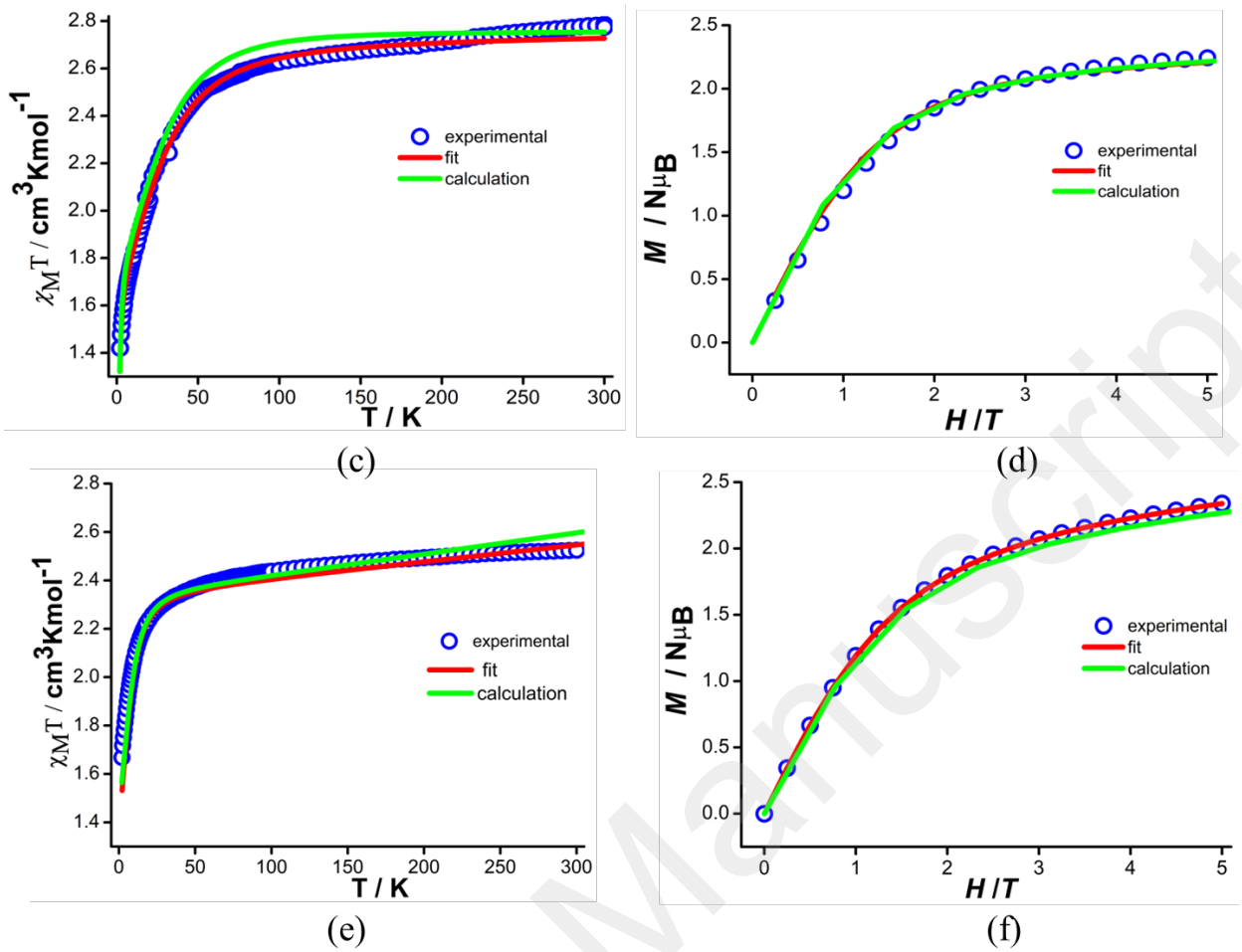

Figure 5. (a, c, e) Temperature-dependent dc magnetic susceptibility plots of **1**–**3**, respectively; (b, d, f) Field-dependent magnetization plots for **1**–**3** respectively at 2K. The solid red lines in all the panels represent the best fits obtained after simultaneous fitting of the magnetic data of using PHI. The solid green lines in all the panels represent simulations of the experimental magnetic data using the computed SH parameters obtained from CASSCF/NEVPT2 calculation.

In order to extract the spin Hamiltonian (SH) parameters of all the three complexes, we fitted both the χ_MT(T) and the $M(H)$ data simultaneously using PHI code.[59] The following Hamiltonian is used for fitting the data:

$$H = D\left[S_z^2 - \frac{S(S+1)}{3}\right] + E\left(S_x^2 - S_y^2\right) + g\mu_B HS$$ ..... equation (1)

Here, D is the axial ZFS parameter; S_x, S_y, and S_z are the x, y, and z-components of the total spin S respectively and E is the rhombic ZFS parameter. Isotropic g values were employed for all the cases in order to avoid over parameterization. A good agreement between the fitted and calculated parameters, presented in Table 1 was obtained. The parameters are consistent with those reported for other penta-coordinated Co^{II} complexes (see Table S6). For complexes **1** and **2** the data were fitted well only when taking positive D values. Changing the sign of D yielded a poor fitting. This confirms the presence of easy plane anisotropy in both **1** and **2**. In the case of **3**, the positive sign of D produced a good fit of the experimental data along with the negative sign of D also produced fairly good fitting (Figure S3). This is due to the presence of sufficient amount of rhombicity in complex **3**. The observed trend of E/D values (**3**>**1**>**2**), after fitting is slightly different from those obtained from theoretical calculations (**3**>**2**>**1**) (*vide infra*). Generally, bulk magnetic susceptibility studies do not afford accurate information on the magnitude and sign of D and E. Secondly; we have fitted the data with isotropic g values. Therefore, a perfect match of the SH parameters between the theoretically computed values (*vide infra*) and the values extracted from PHI is not expected. Below, we will discuss the results of the theoretical calculations and will analyse the ligand field and its impact on D and E.

Table 1. SH parameters extracted from CASSCF/NEVPT2 and PHI fittings for complexes **1**−**3**.

Complexes	**CASSCF/NEVPT2**			**PHI**		
	1	**2**	**3**	**1**	**2**	**3**
D (cm^{-1})	13.3	36.1	±8.6	17.6	30.5	±7.98
$\|E/D\|$	0.14	0.24	0.32	0.16	0.15	0.29

g_x, g_y, g_z or g_{iso}	2.342, 2.28, 2.159	2.620,2.465, 2.082	2.159,2.238, 2.286	2.293	2.4	2.23
TIP (cm^3mol^{-1})	-	-	-	5×10^{-4}	8×10^{-5}	7×10^{-4}
SOC constant ζ (cm^{-1})	515.0	507.8	516.9	-	-	-
Reduction in ζ [1- ζ/ζ_0] x 100%	3.09%	4.44%	2.73%	-	-	-
Racah Parameter B (cm^{-1})	1000.1	1003.1	997.1	-	-	-
Reduction in B [1 - B/B_0] x100%	6.68%	6.40%	6.97%	-	-	-

None of the three complexes display an out-of-phase signal on AC susceptibility down to 2 K in the absence of external DC field in the frequency range 1-1000 Hz. However, at 2 K, the application of an external DC field induces relaxation processes of the magnetic moment of Co^{II} magnetic moments that appear between 1 and 1000 Hz for the three complexes (Figures S4-S6). For the three complexes, the amplitude of the out-of-phase signal, χ_M'', grows with the magnetic field. An optimum field for which: *i*) the amplitude of χ_M'' is maximum and *ii*) the maximum on the χ_M'' vs frequency curves is at the lowest frequency, can be extracted from Figures S4-S6. For complex **1**, the maximum on the χ_M'' vs frequency curves falls out of the limit of our apparatus (10 kHz) so no quantitative information could be safely extracted. For compound **3**, the optimum field can be estimated around 1600 Oe (Figure S6) but the relaxation is still very fast. Indeed, the maximum disappears out of the frequency window at a temperature as low as 2.4 K (Figure S7). For complex **2**, the optimum field is estimated at 1400 Oe and quantitative analysis can be performed at this field by varying the temperature (Figure S8). The data have been analysed in the framework of the extended Debye model (see ESI, Table S3).[60, 61] The most striking feature is that the non-relaxing fraction of the magnetic susceptibility is almost constant and represents nearly 50% of the

global susceptibility which means that nearly 50% of the magnetic centres are concerned by the relaxation. Since the purity of the sample has been checked (see structural description part of the paper), the other 50 % of the susceptibility might come from another magnetic relaxation process of intermolecular either intramolecular origin even in single-ion metal complexes.[62, 63] The temperature dependence of the relaxation time is represented in Figure 6. The temperature and the magnetic field variations of the relaxation time can be reproduced by the following equation:[64]

$$\frac{1}{\tau} = AH^{m}T + BT^{n} + \tau_0 exp\left(\frac{-\Delta}{T}\right) + \frac{C_1}{1+C_2H^2} \quad \text{..... equation (2)}$$

The first term in the right hand side of the equation refers to *direct* process; second term as *Raman*; third term as *Orbach* and last term represents *tunnelling* process. It must be noted that for Kramer ions, m = 4 and n = 9 (in principle), and only *tunnel* and *direct* processes are field-dependent. It would be meaningless to fit the data with not less than height free parameters. The applied 1400 Oe field allowed to discard the presence of QTM process while the field dependence of the magnetic relaxation time shown that Direct process started to operate at such field (Figure S10). The contribution of the Orbach process can be neglected since the fit of the high temperature range of the Arrhenius plot gave an experimental energy barrier of 25 K which is much lower that the expected value from the computed predictions. Finally, it appeared clearly that the remaining combination of processes is *Raman* and *direct*. Such combination perfectly reproduce the experiment (Figure 6). The best fit is obtained with B = 0.77(15) $s^{-1}K^{-6.35}$, n = 6.35(12) and A = 3.41(4)·10^{-10} $s^{-1}Oe^{-4}K^{-1}$ and m = 4 (fixed) (Figure 6). At high temperatures, the relaxation is governed by the *Raman* process and by the *direct* at low temperatures.

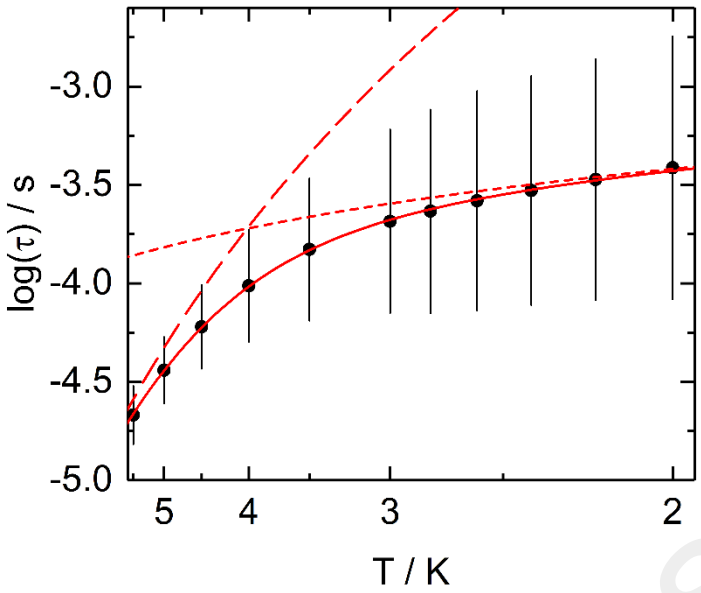

Figure 6. Temperature dependence of the relaxation time for **2** at 1400 Oe in the temperature range of 2-5.5 K with the best-fitted curve (full red line) with the combination *Raman+direct*. The *Raman* contribution to the relaxation time is represented by the long dashed red line and the *direct* shorts dashes. Error lines are calculated using the log-normal distribution model at the 1σ level.[65]

To probe the effect of close packing of magnetic molecules in the condensed phase, the zinc (II) analogues of **1**-**2** were prepared. We found that the zinc (II) analogues of **1** crystallized in a space group that was different (see Table S2). Hence, dilution experiments on **1** were not carried out. The zinc(II) analogue of **2**, which is isomorphous to **2**, was doped with ~10% of Co^{II} to prepare $\mathbf{2_{10}}$. The exact doping ratio (6.5%) is easily determined from the magnetization curve at 2 K and the thermal dependence of the magnetic susceptibility (Figures S11) that is compared to **2**. Like **2**, $\mathbf{2_{10}}$ does not exhibit any out-of-phase signal in the absence of external DC but a maximum progressively appears on the χ_M'' vs. frequency curves at 2 K with the application of an external field (Figure S12). However, this maximum appears at a frequency ten times smaller than in the pure condensed crystalline phase with nearly the same optimum field (1600 Oe) and quantitative analysis can be performed at this

field by varying the temperature (Table S4, Figure S13). Extended Debye model applied to the field variations of the AC susceptibility vs. frequency plots provides the thermal variation of the relaxation time observed (Table S5, Figure 7).

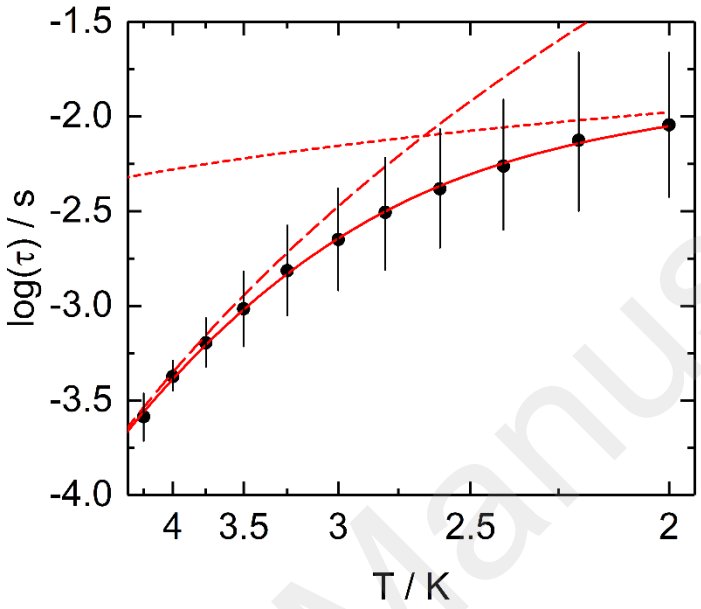

Figure 7. Temperature dependence of the relaxation time for $\mathbf{2_{10}}$ at 1600 Oe in the temperature range of 2-4.25 K with the best-fitted curve (full red line) with the combination *Raman+direct*. The *Raman* contribution to the relaxation time is represented by the long dashed red line and the *direct* shorts dashes. Error lines are calculated using the log-normal distribution model at the 1σ level.[65]

The presence of 1600 Oe applied magnetic field and the field dependence of the relaxation time (Figure S13) for $\mathbf{2_{10}}$ are in favour of the absence of QTM and the existence of Direct processes. One more time the experimental energy barrier extracted from the high temperature range (29 K) is smaller than the calculated value and then the Orbach contribution is negligible. Thus the combination of *Raman* and *direct* processes, like for **2**, perfectly reproduces the experiment. The best fit is obtained with B = 0.13(3) $s^{-1}K^{-7.02}$, n =

7.0(2) and A = 7.3(3)·10^{-12} $s^{-1}Oe^{-4}K^{-1}$ and m = 4 (fixed) (Figure 7). The main difference between the relaxation time of the doped (**2_{10}**) and the pure (**2**) compounds lies in the evolution of the direct process which is, roughly, ten times smaller in **2_{10}** than in **2** in the whole temperature range.

Computational studies of 1-3

To obtain insight into the electronic structure and magnetic properties, we have performed *ab initio* CASSCF-NEVPT2 calculations. These methodologies have a proven track record of yielding good numerical accuracy for the zero-field splitting parameters for transition metal systems (see Computational Details for further information)[41, 66-70].

The computed Spin-Hamiltonian parameters, *D*, *E*/*D*, g_x, g_y and g_z, for the three complexes are reported in Table 1. For complexes **1** and **2**, the *D* value is found to be +13.3 and +36.1 cm^{-1} respectively, whereas in case of complex **3**, the magnitude of *D* is estimated to be 8.6 cm^{-1} (*E*/*D* is 0.32) although the sign of *D* could not be determined unambiguously. The calculated *g* values indicate a significant anisotropy.[71] With these computed ZFS parameters, the experimental DC plots have been simulated which reveals an excellent match with the theoretical values (see Figure 5).

The magnitude of the *D* values increases from 13.3 cm^{-1} in complex **1** to 36.1 cm^{-1} in complex **2** but decrease to 8.6 cm^{-1}in **3**. The sign and magnitude of the *D* values of the three complexes can be described by the following equation:[72]

$$D_{ij} = -\frac{\zeta^2}{4S^2}\sum_{p,q}\frac{\langle\Psi_p|\hat{l}_i|\Psi_q\rangle\langle\Psi_q|\hat{l}_j|\Psi_p\rangle}{\varepsilon_q-\varepsilon_p} \qquad \text{……equation (3)}$$

Where D_{ij} is the diagonalized and traceless matrix components derived from second-order perturbation of spin-orbit coupling (SOC), ζ is the effective SOC constant of Co^{II} in the

molecular environment, Ψp, Ψq are the ground- and excited state wave functions arising from same spin value *S* and ε_p, ε_q are their corresponding energies respectively. By looking at the NEVPT2 computed excited electronic states, it is clear that the first four or five excited states contribute considerably to the overall *D* value in all the three complexes (see Tables S7-S9 and Figure S15). A very simple correlation can be made in terms of the magnitude of *D* with the NEVPT2 estimated ground-excited state gaps, as the *D* value is inversely proportional to the energy difference between the states. Thus, the *D* value increases from complex **1** to complex **2** because the ligand field strength decreases from Cl to Br and hence the excited states come closer for the compound containing bromide ligand compared to the chloride analogue. This heavy atom effects on anisotropy has been studied in detail, while here it is found to influence the *D* significantly, in other cases structural distortions found to play a prominent role.[70, 73]

For a deeper understanding of the sign and state-wise contribution to the *D* and *E* values, we have plotted the ligand field d-orbital splitting of all the three complexes and tabulated the major state-wise contributions (see Figure 8 and Tables S7 to S9). Here an important observation is that due to the absence of axial anisotropy and the presence of significant rhombicity, most of the electronic states are multi-configurational, *i.e.*, none of them can be described by a single determinant[74] and this suggests a strong mixing among d-orbitals due to lower symmetry (see Figure S16 in ESI). For this reason, the computed d-orbital splitting differs from that expected for an ideal TBP or SP geometries.

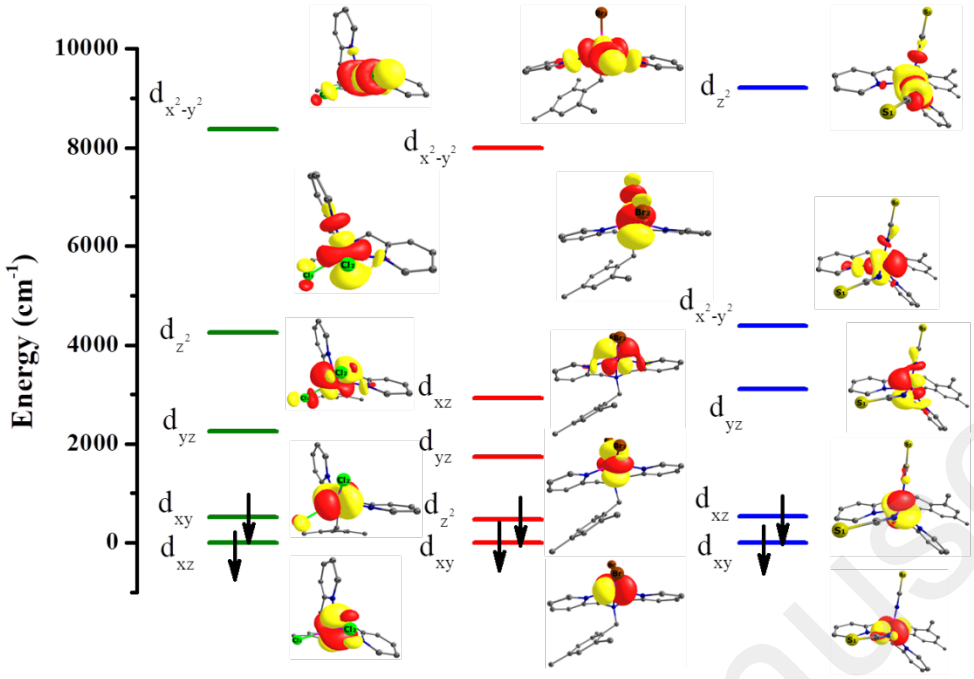

Figure 8. Computed ligand field d-orbital splitting diagrams for complexes **1**(left), **2** (middle) and **3** (right).

In the case of complexes **1** and **2**, the major positive contribution towards the *D* value arises from the first and second excited states. These are 14.2 and 9.7 cm^{-1} for **1;** 22.7 and 29.2 cm^{-1} for **2** (see Tables S7 and S9). For complex **1**, these two excited states arise from the electronic transitions of different M_L levels *i.e.* $d_{xz} \rightarrow d_z^2$ and $d_{xy} \rightarrow d_{yz}$. The orbital splitting pattern changes significantly on moving to complex **2** and here $d_z^2 \rightarrow d_{xz}/d_{yz}$ and $d_{xy} \rightarrow d_{yz}/d_{xz}$ electronic transition is responsible for the generation of first and second excited states. Both **1**-**2** also have some negative contribution to the *D* value arising from $d_{xy} \rightarrow d_{x^2-y^2}$ transition possessing the same M_L value of -12 cm^{-1} for **1**-**2** (see Tables S7 and S8).

In the case of **3** as the rhombicity is very high (E/D = 0.32) and therefore the sign of *D* could not be determined unambiguously. Calculations, however, yield a negative sign to the *D* value. Furthermore, the ligand field splitting in the case of **3** is found to be higher compared

to **1** and **2** in line with the expectations. Here the major contributions to the *D* value arise from dominant $d_{xy} \rightarrow d_{x^2-y^2}$ and $d_{xz} \rightarrow d_{yz}$ (same M_L transitions) transitions from first and the second excited states with a contribution of -9.3 and -5.1 cm^{-1}, respectively. Additionally, there is also a significant positive contribution towards *D* (7.6 cm^{-1}) from 4th excited state where $d_{xz} \rightarrow d_{z^2}$ transition dominates.

Additionally, we have also performed *ab initio* ligand field theory (AILFT) calculations on complexes **1**-**3** to obtain insight into the nature of metal-ligand bonding by computing the nephelauxetic reduction in Racah parameter (B) and spin-orbit coupling constant parameter (ζ) with 10 quartet states. These values are compared to the value obtained for free ion Co^{II} by calculating the same at the same level of theory (ζ_0 is 531.4 cm^{-1} and B_0 is 1071.7 cm^{-1} for free Co(II) ion).[75] The computed values are given in Table 1. It is clear that the nephelauxetic reduction in ζ parameter is higher for complex **2** compared to **1** and **3** and this is related to the smaller ligand field splitting observed for this complex compared to the other two complexes. This also correlated to the largest *D* value obtained. The nephelauxetic reduction in Racah parameter, however, reveals that the largest reduction is on complex **3** compared to **1** and **2**. This essentially indicates stronger metal-ligand covalency due to the presence of thiocyanide ligand.

Conclusion

In conclusion, we have synthesised three new mononuclear pentacoordinate Co^{II} complexes (**1**-**3**). The geometry around Co^{II} in **1** and **3** is close to TBP while for **2** the geometry is much closer to square pyramid. Both DC and AC magnetic measurements were carried out on the complexes. The extracted spin Hamiltonian parameters from the DC magnetic data indicate the presence of an easy plane magnetic anisotropy in the case of complexes **1** and **2** with a positive sign of *D*. In the case of **3** the sign of *D* could not be determined unambiguously as

the *E*/*D* value is close to the rhombicity limit of 0.33. This finding is further proved by the detailed NEVPT2 calculations. AC magnetic measurements showed the absence of any zero-field single-ion magnet behaviour for all the complexes. After finding an optimum field (around 1400 Oe) and applying it, slow relaxation of magnetisation was observed. However, for complexes **1** and **3** the relaxation was too fast even after applying the optimum field to extract the value of the energy barrier for magnetic reversal and other parameters. For complex **2** in the presence of the optimum field, peak maxima in the out-of-phase susceptibility curves were observed which enabled extraction of data. The slow relaxation in **2** is mainly governed by the *Raman* and the *direct* processes. Theoretical calculations showed that most of the electronic states in the complexes are multifunctional and cannot be described by a single determinant. This mixing explains the fast reversal of the magnetization of the complexes as well as the absence of the zero-field SIM behaviour. This effect is also attributed to the deviation from perfect trigonal bipyramidal (TBP) or square pyramidal (SP) geometries of the complexes. The calculated orbital energy ordering showed that the different M_L level electronic transitions are responsible for the positive sign of the *D* values. Paralally, from the ligand-field splitting pattern, it is evident that as the donor strength of the coordinated anioninc ligands increases from Br^- <Cl^- <SCN^- (or **2**<**1**<**3**) the |*D*| value decreases as $|D_{Br}| > |D_{Cl}| > |D_{NCS}|$ and this infers that soft donor atoms can induce higher zero-field splitting for the complexes. *Ab initio* ligand field theory (AILFT) calculations disclosed that the spin-orbit coupling constant parameter (ζ) is highest for **2** leading to the highest *D* value among the three complexes. Also, the reduction in the Racah parameter is highest for **3** indicating stronger metal-ligand covalency with the thiocyanide ligand. This study is one more step towards achieving an understanding of the influence of ligand field on spin Hamiltonian parameters and magnetization dynamics in mononuclear Co^{II} complexes.

Conflicts of interest

The authors declare no competing financial interest.

Acknowledgments

VC thanks the Department of Science and Technology (DST), India for J. C. Bose fellowship and also support for the Single Crystal CCD X-ray Diffractometer facility at IIT-Kanpur. FP thanks the CNRS, Université de Rennes 1, and the European Commission through the ERC-CoG 725184 MULTIPROSMM (project no. 725184) for financial support. J.A. thanks the Department of Science and Technology (DST), India for INSPIRE Senior Research Fellowship. JA is thankful to Mr. Shovon Chatterjee, IIT Kanpur and Ms. Navaneetha T, University of Hyderabad for collecting PXRD data of the complexes. AS would like to acknowledge CSIR for SRF fellowship and G.R. would like to thank SERB, India for funding (CRG/2018/000430).

References

1. M. Feng and M.-L. Tong, *Chem.-Eur. J.*, 2018, **24**, 7574-7594.
2. M. Gregson, N. F. Chilton, A.-M. Ariciu, F. Tuna, I. F. Crowe, W. Lewis, A. J. Blake, D. Collison, E. J. L. McInnes, R. E. P. Winpenny and S. T. Liddle, *Chem. Sci.*, 2016, **7**, 155-165.
3. F.-S. Guo, A. K. Bar and R. A. Layfield, *Chem. Rev.*, 2019, **119**, 8479-8505.
4. F.-S. Guo, B. M. Day, Y.-C. Chen, M.-L. Tong, A. Mansikkamäki and R. A. Layfield, *Angew. Chem. Int. Ed.*, 2017, **56**, 11445-11449.
5. A. F. R. Kilpatrick, F.-S. Guo, B. M. Day, A. Mansikkamäki, R. A. Layfield and F. G. N. Cloke, *Chem. Commun.*, 2018, **54**, 7085-7088.

6. K. Randall McClain, C. A. Gould, K. Chakarawet, S. J. Teat, T. J. Groshens, J. R. Long and B. G. Harvey, *Chem. Sci.*, 2018, **9**, 8492-8503.

7. R. Bagai and G. Christou, *Chem. Soc. Rev.*, 2009, **38**, 1011-1026.

8. R. Sessoli, H. L. Tsai, A. R. Schake, S. Wang, J. B. Vincent, K. Folting, D. Gatteschi, G. Christou and D. N. Hendrickson, *J. Am. Chem. Soc.*, 1993, **115**, 1804-1816.

9. N. Ishikawa, M. Sugita, T. Ishikawa, S.-y. Koshihara and Y. Kaizu, *J. Am. Chem. Soc.*, 2003, **125**, 8694-8695.

10. J. D. Rinehart and J. R. Long, *Chem. Sci.*, 2011, **2**, 2078-2085.

11. S. K. Gupta, T. Rajeshkumar, G. Rajaraman and R. Murugavel, *Chem. Sci.*, 2016, **7**, 5181-5191.

12. Y.-S. Ding, N. F. Chilton, R. E. P. Winpenny and Y.-Z. Zheng, *Angew. Chem. Int. Ed.*, 2016, **55**, 16071-16074.

13. C. A. P. Goodwin, F. Ortu, D. Reta, N. F. Chilton and D. P. Mills, *Nature*, 2017, **548**, 439.

14. F.-S. Guo, B. M. Day, Y.-C. Chen, M.-L. Tong, A. Mansikkamäki and R. A. Layfield, *Science*, 2018, **362**, 1400-1403.

15. P. E. Kazin, M. A. Zykin, Y. V. Zubavichus, O. V. Magdysyuk, R. E. Dinnebier and M. Jansen, *Chem.-Eur. J.*, 2014, **20**, 165-178.

16. J. M. Zadrozny, M. Atanasov, A. M. Bryan, C.-Y. Lin, B. D. Rekken, P. P. Power, F. Neese and J. R. Long, *Chem. Sci.*, 2013, **4**, 125-138.

17. D. Weismann, Y. Sun, Y. Lan, G. Wolmershäuser, A. K. Powell and H. Sitzmann, *Chem.-Eur. J.*, 2011, **17**, 4700-4704.

18. U. Chakraborty, S. Demeshko, F. Meyer, C. Rebreyend, B. de Bruin, M. Atanasov, F. Neese, B. Mühldorf and R. Wolf, *Angew. Chem. Int. Ed.*, 2017, **56**, 7995-7999.

19. P. P. Samuel, K. C. Mondal, H. W. Roesky, M. Hermann, G. Frenking, S. Demeshko, F. Meyer, A. C. Stückl, J. H. Christian, N. S. Dalal, L. Ungur, L. F. Chibotaru, K. Pröpper, A. Meents and B. Dittrich, *Angew. Chem. Int. Ed.*, 2013, **52**, 11817-11821.

20. Y.-S. Meng, Z. Mo, B.-W. Wang, Y.-Q. Zhang, L. Deng and S. Gao, *Chem. Sci.*, 2015, **6**, 7156-7162.

21. X.-N. Yao, J.-Z. Du, Y.-Q. Zhang, X.-B. Leng, M.-W. Yang, S.-D. Jiang, Z.-X. Wang, Z.-W. Ouyang, L. Deng, B.-W. Wang and S. Gao, *J. Am. Chem. Soc.*, 2017, **139**, 373-380.

22. P. C. Bunting, M. Atanasov, E. Damgaard-Møller, M. Perfetti, I. Crassee, M. Orlita, J. Overgaard, J. van Slageren, F. Neese and J. R. Long, *Science*, 2018, **362**, eaat7319.

23. J. M. Zadrozny, D. J. Xiao, M. Atanasov, G. J. Long, F. Grandjean, F. Neese and J. R. Long, *Nat. Chem.*, 2013, **5**, 577.

24. R. C. Poulten, M. J. Page, A. G. Algarra, J. J. Le Roy, I. López, E. Carter, A. Llobet, S. A. Macgregor, M. F. Mahon, D. M. Murphy, M. Murugesu and M. K. Whittlesey, *J. Am. Chem. Soc.*, 2013, **135**, 13640-13643.

25. R. Herchel, L. Váhovská, I. Potočňák and Z. Trávníček, *Inorg. Chem.*, 2014, **53**, 5896-5898.

26. Y. Rechkemmer, F. D. Breitgoff, M. van der Meer, M. Atanasov, M. Hakl, M. Orlita, P. Neugebauer, F. Neese, B. Sarkar and J. van Slageren, *Nat. Commun.*, 2016, **7**, 10467.

27. S. Vaidya, S. Tewary, S. K. Singh, S. K. Langley, K. S. Murray, Y. Lan, W. Wernsdorfer, G. Rajaraman and M. Shanmugam, *Inorg. Chem.*, 2016, **55**, 9564-9578.

28. S. Vaidya, S. K. Singh, P. Shukla, K. Ansari, G. Rajaraman and M. Shanmugam, *Chem.-Eur. J.*, 2017, **23**, 9546-9559.

29. A. V. Palii, D. V. Korchagin, E. A. Yureva, A. V. Akimov, E. Y. Misochko, G. V. Shilov, A. D. Talantsev, R. B. Morgunov, S. M. Aldoshin and B. S. Tsukerblat, *Inorg. Chem.*, 2016, **55**, 9696-9706.

30. D. V. Korchagin, A. V. Palii, E. A. Yureva, A. V. Akimov, E. Y. Misochko, G. V. Shilov, A. D. Talantsev, R. B. Morgunov, A. A. Shakin, S. M. Aldoshin and B. S. Tsukerblat, *Dalton Trans.*, 2017, **46**, 7540-7548.

31. R. Díaz-Torres, M. Menelaou, O. Roubeau, A. Sorrenti, G. Brandariz-de-Pedro, E. C. Sañudo, S. J. Teat, J. Fraxedas, E. Ruiz and N. Aliaga-Alcalde, *Chem. Sci.*, 2016, **7**, 2793-2803.

32. J. Vallejo, I. Castro, R. Ruiz-García, J. Cano, M. Julve, F. Lloret, G. De Munno, W. Wernsdorfer and E. Pardo, *J. Am. Chem. Soc.*, 2012, **134**, 15704-15707.

33. J. Vallejo, E. Pardo, M. Viciano-Chumillas, I. Castro, P. Amorós, M. Déniz, C. Ruiz-Pérez, C. Yuste-Vivas, J. Krzystek, M. Julve, F. Lloret and J. Cano, *Chem. Sci.*, 2017, **8**, 3694-3702.

34. J. Acharya, A. Swain, A. Chakraborty, V. Kumar, P. Kumar, J. F. Gonzalez, O. Cador, F. Pointillart, G. Rajaraman and V. Chandrasekhar, *Inorg. Chem.*, 2019, **58**, 10725-10735.

35. S. Vaidya, P. Shukla, S. Tripathi, E. Rivière, T. Mallah, G. Rajaraman and M. Shanmugam, *Inorg. Chem.*, 2018, **57**, 3371-3386.

36. A. K. Mondal, J. Jover, E. Ruiz and S. Konar, *Dalton Trans.*, 2019, **48**, 25-29.

37. A. K. Mondal, A. Mondal, B. Dey and S. Konar, *Inorg. Chem.*, 2018, **57**, 9999-10008.

38. J. M. Zadrozny and J. R. Long, *J. Am. Chem. Soc.*, 2011, **133**, 20732-20734.

39. A. Eichhöfer, Y. Lan, V. Mereacre, T. Bodenstein and F. Weigend, *Inorg. Chem.*, 2014, **53**, 1962-1974.

40. L. Chen, J. Wang, J.-M. Wei, W. Wernsdorfer, X.-T. Chen, Y.-Q. Zhang, Y. Song and Z.-L. Xue, *J. Am. Chem. Soc.*, 2014, **136**, 12213-12216.

41. M. A. Hay, A. Sarkar, G. A. Craig, L. Bhaskaran, J. Nehrkorn, M. Ozerov, K. E. R. Marriott, C. Wilson, G. Rajaraman, S. Hill and M. Murrie, *Chem. Sci.*, 2019, **10**, 6354-6361.

42. A. I. F. Vogel, B. S.; Hannaford, A. J.; Smith, P. W. G.; Tatchell, A. R., *Vogel's textbook of practical organic chemistry*, 5th ed. edn., **1989**.

43. *Bruker Analytical X-ray Systems,I. M., WI, SMART & SAINT Software Reference Manuals*, **2003**.

44. *Sheldrick, G. M. SADABS: A software for empirical absorption correction, Ver. 2.05*, University of Göttingen, Göttingen, Germany, **2002**.

45. *SHELXTL Reference Manual*, Bruker Analytical X-ray Systems, Inc.: Madison, WI, **2000**.

46. *CrysAlis PRO, Rigaku Oxford Diffraction*, Yarnton, England., **2015**.

47. G. Sheldrick, *Acta Crystallogr. A*, 2008, **64**, 112-122.

48. O. V. Dolomanov, L. J. Bourhis, R. J. Gildea, J. A. K. Howard and H. Puschmann, *Journal of Applied Crystallography*, 2009, **42**, 339-341.

49. K. Bradenburg, *Diamond, Ver. 3.1eM, Crystal Impact GbR*, Bonn, Germany, **2005**.

50. F. Neese, *Wiley Interdiscip. Rev. Comput. Mol. Sci.*, 2018, **8**, e1327.

51. R. Maurice, R. Bastardis, C. d. Graaf, N. Suaud, T. Mallah and N. Guihéry, *J. Chem. Theory Comput.*, 2009, **5**, 2977-2984.

52. T. Jurca, A. Farghal, P.-H. Lin, I. Korobkov, M. Murugesu and D. S. Richeson, *J. Am. Chem. Soc.*, 2011, **133**, 15814-15817.

53. A. K. Mondal, T. Goswami, A. Misra and S. Konar, *Inorg. Chem.*, 2017, **56**, 6870-6878.

54. F. Habib, O. R. Luca, V. Vieru, M. Shiddiq, I. Korobkov, S. I. Gorelsky, M. K. Takase, L. F. Chibotaru, S. Hill, R. H. Crabtree and M. Murugesu, *Angew. Chem. Int. Ed.*, 2013, **52**, 11290-11293.

55. I. Hargittai, *Angewandte Chemie International Edition in English*, 1997, **36**, 2525-2525.

56. H. Zabrodsky, S. Peleg and D. Avnir, *J. Am. Chem. Soc.*, 1992, **114**, 7843-7851.

57. C. R. Martinez and B. L. Iverson, *Chem. Sci.*, 2012, **3**, 2191-2201.

58. C. Harris, T. Lockyer, R. Martin, H. Patil and E. Sinn, *Aust. J. Chem.*, 1969, **22**, 2105-2116.

59. N. F. Chilton, R. P. Anderson, L. D. Turner, A. Soncini and K. S. Murray, *J. Comput. Chem.*, 2013, **34**, 1164-1175.

60. C. Dekker, A. F. M. Arts, H. W. de Wijn, A. J. van Duyneveldt and J. A. Mydosh, *Phys. Rev. B*, 1989, **40**, 11243-11251.

61. K. S. Cole and R. H. Cole, *J. Chem. Phys.*, 1941, **9**, 341-351.

62. L. T. A. Ho and L. F. Chibotaru, *Phys. Rev. B*, 2016, **94**, 104422.

63. L. T. A. Ho and L. F. Chibotaru, *Phys. Rev. B*, 2018, **98**, 174418.

64. P. Z. Jinkui Tang, *Lanthanide Single Molecule Magnets*, Spinger, **2015**.

65. D. Reta and N. F. Chilton, *Phys. Chem. Chem. Phys.*, 2019, **21**, 23567-23575.

66. D. Schweinfurth, M. G. Sommer, M. Atanasov, S. Demeshko, S. Hohloch, F. Meyer, F. Neese and B. Sarkar, *J. Am. Chem. Soc.*, 2015, **137**, 1993-2005.

67. B. Cahier, R. Maurice, H. Bolvin, T. Mallah and N. Guihéry, *Magnetochemistry*, 2016, **2**, 31.

68. D. Schweinfurth, J. Krzystek, M. Atanasov, J. Klein, S. Hohloch, J. Telser, S. Demeshko, F. Meyer, F. Neese and B. Sarkar, *Inorg. Chem.*, 2017, **56**, 5253-5265.

69. F. Shao, B. Cahier, E. Rivière, R. Guillot, N. Guihéry, V. E. Campbell and T. Mallah, *Inorg. Chem.*, 2017, **56**, 1104-1111.

70. G. Rajaraman, A. Sarkar, S. Tewary and S. Sinkar, *Chem.: Asian J.*, 2014, **14**, 4696-4704.

71. M. Atanasov, D. Aravena, E. Suturina, E. Bill, D. Maganas and F. Neese, *Coord. Chem. Rev.*, 2015, **289-290**, 177-214.

72. S. Gomez-Coca, E. Cremades, N. Aliaga-Alcalde and E. Ruiz, *J. Am. Chem. Soc.*, 2013, **135**, 7010-7018.

73. E. A. Suturina, D. Maganas, E. Bill, M. Atanasov and F. Neese, *Inorg. Chem.*, 2015, **54**, 9948-9961.

74. R. Ruamps, L. J. Batchelor, R. Guillot, G. Zakhia, A.-L. Barra, W. Wernsdorfer, N. Guihéry and T. Mallah, *Chem. Sci.*, 2014, **5**, 3418-3424.

75. S. K. Singh, J. Eng, M. Atanasov and F. Neese, *Coord. Chem. Rev.*, 2017, **344**, 2-25.

“For Table of Contents Use Only”

Influence of Ligand Field on Magnetic Anisotropy in a Family of Pentacoordinate Co^{II} Complexes

Joydev Acharya,[a] Arup Sarkar,[b] Pawan Kumar,[a] Vierandra Kumar,[a] Jessica Flores Gonzalez,[c] Olivier Cador,[c] Fabrice Pointillart,[c] Gopalan Rajaraman,*[b] and Vadapalli Chandrasekhar*[a,d]*

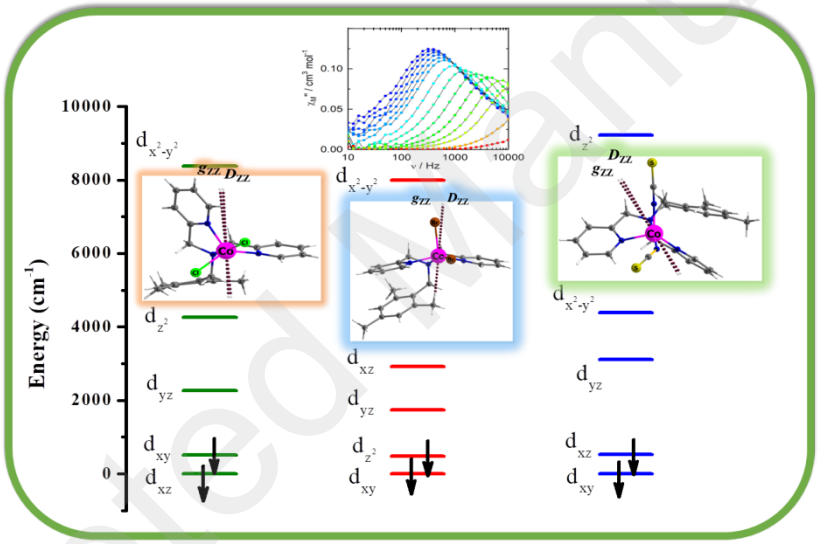

Three pentacoordinate Co^{II} complexes were synthesized using a common tridentate ligand and varying the halide/pseudohalide ligand. The effect of the latter on the geometry and magnetic properties of the three complexes has been analysed.